International Journal of Engineering, Mathematical and Physical Sciences
ISSN: 2517-9934
Vol:6, No:8, 2012

Design Optimization of Aerocapture with Aerodynamic-Environment-Adaptive Variable Geometry Flexible Aeroshell

Naohiko Honma, Kojiro Suzuki

***Abstract*—**This paper proposes the concept of aerocapture with aerodynamic-environment-adaptive variable geometry flexible aeroshell that vehicle deploys. The flexible membrane is composed of thin-layer film or textile as its aeroshell in order to solve some problems obstructing realization of aerocapture technique. Multi-objective optimization study is conducted to investigate solutions and derive design guidelines. As a result, solutions which can avoid aerodynamic heating and enlarge the corridor width up to 10% are obtained successfully, so that the effectiveness of this concept can be demonstrated. The deformation-use optimum solution changes its drag coefficient from 1.6 to 1.1, along with the change in dynamic pressure. Moreover, optimization results show that deformation-use solution requires the membrane for which upper temperature limit and strain limit are more than 700 K and 120%, respectively, and elasticity (Young's modulus) is of order of 10^6 Pa.

***Keywords*—**Aerocapture, flexible aeroshell, optimization, response surface methodology.

I. Introduction

IN recent years, planetary exploration including the Mars and Moon has become an international point of interest. Particularly, the Mars attracts people's attention because it has scientifically interesting topics as a terrestrial planet. In addition, Mars exploration is challenging also in engineering field that various kind of probes have been sent on Mars so far. Although 42 exploration missions were carried out, success was less than 50%. The establishment of low cost, highly reliable and efficient space transportation system and orbit insertion technique for Mars or other planets seems to be an urgent task. Orbit insertion technique that uses orbital maneuvering engine of specific impulse (I_{sp}) of more than 315 sec has been established so far [1]. However, such a conventional orbit insertion technique that uses the chemical propulsion system imposes a constraint that a large amount of chemical propellant for deceleration should be equipped through the trip from launch to arrival. This would put a limitation to the payload mass for scientific instruments essentially needed for observations. For example, if a spacecraft leaves Low Earth Orbit (LEO) of 400 km and it is inserted into circular orbit of 500 km around Mars, the required fuel mass fraction for deceleration becomes 48% assuming that I_{sp} is 315 sec. Compared with such a conventional technique, the aerocapture technique [2] has the potential for providing substantial fuel consumption savings, because aerodynamic drag is used to remove enough kinetic energy by deceleration, with only a single atmospheric entry. It also enables us to complete orbital maneuvering in shorter time than aerobraking, which takes several weeks or several months to insert the vehicle into the target orbit. Therefore, aerocapture technique is effective especially for the mission where weight and time limitations are significantly severe.

Naohiko Honma is doctoral student at the Department of Advanced Energy, Graduate School of Frontier Sciences, The University of Tokyo, Japan. (e-mail: honma@daedalus.k.u-tokyo.ac.jp).

Kojiro Suzuki is Professor at the Department of Advanced Energy, Graduate School of Frontier Sciences, The University of Tokyo, Japan. (e-mail: kjsuzuki@daedalus.k.u-tokyo.ac.jp).

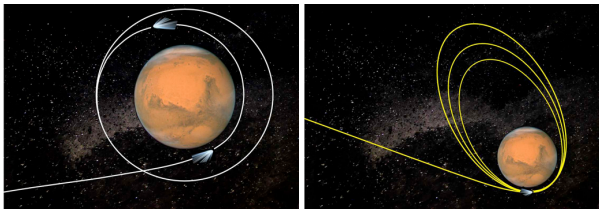

(a) (b)

Fig. 1 (a)Aerocapture, (b)Aerobrake

However, aerocapture mission involves a lot of complicated technical difficulties. For example, the aerodynamic heating must be taken into account as one of the most critical problems in aerocapture mission. Thermal protection system (TPS) should be installed on aerocapture vehicle. However, usual TPS is not reusable and it requires high reliability, thus cost for both development and repair becomes significant. In addition, allowable width of atmospheric entry path angle, what is called as "corridor", is quite narrow. Here, corridor is defined as the width of flight path angle between shallowest entry angle and deepest entry angle. Too deep entry angle results in crash onto the ground, on the other hand, too shallow entry angle causes lack of deceleration thus vehicle goes back to the hyperbolic orbit. Such a quite narrow corridor width requires very high accuracy of guidance, navigation and control (GNC) system, because error in entry angle offers a considerably high risk on mission. It is necessary not only to improve the accuracy of GNC, but also to enable the vehicle to absorb such errors even after entering the atmosphere. One of the means to give the robustness against such an error or uncertainty is lift or drag modulation during atmospheric flight. Appropriate lift or drag modulation adjusts the descending and ascending rate without losing necessary deceleration. As a result, the vehicle can avoid the crash onto the ground. Conventional Mars aerocapture mission analysis [3] considered on-board guidance and control system with moderate lift-to-drag ratio (L/D) to have the robustness. However, this kind of system requires a GNC subsystem that is composed of on-board computers and sophisticated attitude control device such as body flap or thrusters for

reaction control system, thereby involving the risk of increase of equipment failure or development cost.

In order to solve these problems, this paper proposes the aerodynamic-environment-adaptive variable geometry flexible aeroshell concept where aerocapture vehicle deploys the flexible membrane composed of thin-layer film or textile as its aeroshell. Unlike conventionally proposed aerocapture design, this concept aims not to "protect from" but to "avoid" heating, and also, aims not to "intellectually" control by using on-board computer and sophisticated aero-device but to "non-intellectually" and autonomously adapt to the surrounding environment and absorb some errors or uncertainties. This research shows its potential to become the breakthrough for severe aerodynamic heating and uncertain errors. First of all, aeroshell composed of large membrane becomes very lightweight and foldable that a vehicle can decelerate at higher altitude where atmospheric density is very low, thanks to a large but low-mass aeroshell. Therefore, a vehicle is able to avoid aerodynamic heating. A deployable and flexible aeroshell made by thermally resistant textile has the potential for realizing a low ballistic coefficient aerocapture vehicle. Secondarily, taking advantage of the deformability of flexible membrane certainly has possibility to give the robustness against error in entry angle. For example, when a vehicle enters the atmosphere at a deeper angle than having planned, it goes down to a lower altitude, it experiences much higher dynamic pressure rather than expected. However, by changing the form of membrane so that drag coefficient is lowered adaptively to such environment, the resultant drag force could be kept constant. In this way, if the flexible vehicle is able to change its body form according to dynamic pressure or temperature adaptively, dispersion of errors in entry angle is absorbed and thus robustness can be given to the vehicle. This proposition gives the new design concept for aerocapture, which is robust, reliable, simple, low cost, and reusable. Some concepts aiming at avoiding aerodynamic heating by using thermally-resistant membrane, which can realize lightweight and large area, have been proposed in various organizations [4]-[6], however, concepts which added robustness to the vehicle by taking advantage of deformability of membrane have never been proposed so far. This becomes a complicated design problem because multi-disciplinary domains such as aerodynamics, structure, and trajectory are related with each other closely, thus deriving the design guidelines is an important issue. In this paper, multi objective optimization study is conducted to search solutions avoiding aerodynamic heating and having robustness against errors, and to show the effectiveness of this concept.

Fig. 2 shows a schematic of aerocapture flight profile. The vehicle approaches Mars from a hyperbolic approach trajectory, shown at point 1, and then enters the atmospheric interface, shown at point 2. From point 3 to point 6, the drag on the vehicle provides the deceleration, which is required to capture the vehicle into the desired orbit. At point 7 and 8, small delta-V burning is performed to raise the periapsis and to circularize the vehicle around the planet, respectively. This research considered the following Mars aerocapture mission. The vehicle approaches the Martian atmosphere at an entry speed of 5.7 km/s at an altitude of 120 km, which is calculated using patched conic approximation [7], and the gross weight is 1200 kg. The target orbit is set to be 500 km [8], which is a circular science observation orbit. Because the orbit after escaping from atmosphere is changed according to the aerodynamic coefficient and flight trajectory, the spacecraft must perform a small delta-V burning at the apoapsis (point 7) and periapsis (point 8) to insert spacecraft into the target orbit.

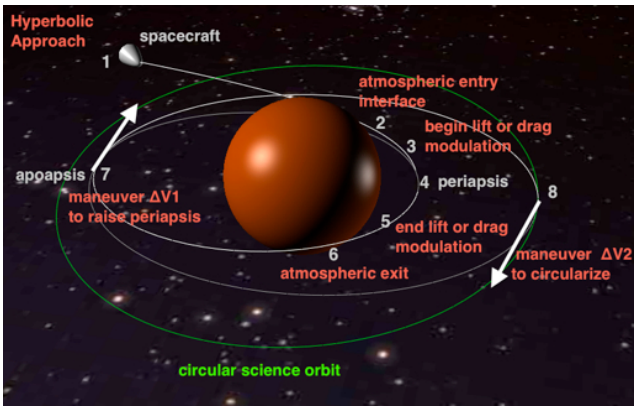

Fig. 2 Mars aerocapture mission schematic

II. Models

A. Formulation of Optimization Problem

In this section, optimization problem for variable-geometry- aeroshell-aerocapture mission is formulated. In a certain dynamic system, defining the state vector $\mathbf{x}(t) \in R^m$ and design vector $\mathbf{d}(t) \in R^M$, which are the time dependent variables, state equation of this system is given as (1).

$$\dot{\mathbf{x}}(t) = f\left(\mathbf{x}(t), \mathbf{d}(t)\right) \tag{1}$$

Three degrees of freedom equations of motion for point mass is considered as a state equation (1) as shown in (2) through (7). For simplicity of analysis, Mars is assumed to be perfectly spherical and the rotation effect is neglected. In addition, thruster is not used when flying through the planet's atmosphere. Thruster is only used at the apoapsis (point 7) and periapsis (point 8). Fig. 3 shows the spherical coordinates for the state equation.

$$\dot{r} = V\sin\gamma \tag{2}$$

$$\dot{\theta} = V\cos\gamma\cos\psi / r\cos\phi \tag{3}$$

$$\dot{\phi} = V\cos\gamma\sin\psi / r \tag{4}$$

$$\dot{V} = -D/m - g\sin\gamma \tag{5}$$

$$\dot{\gamma} = (L/mV)\cos\beta - (g/V - V/\gamma)\cos\gamma \tag{6}$$

$$\dot{\psi} = (L/mV) - \sin\beta/\cos\gamma - V\cos\gamma\tan\phi\cos\psi / r \tag{7}$$

where,

$$g = \mu / r^2 \tag{8}$$

$$L = qC_L S_{ref} \tag{9}$$

$$D = qC_D S_{ref} \tag{10}$$

$r[m]$: distance form planet center, $V[m/s]$: velocity,
$\gamma[rad]$: flight path angle, $\theta[rad]$: longitude
$\psi[rad]$: azimuth angle, $\phi[rad]$: latitude, $D[N]$: drag
$m[kg]$: mass, $L[N]$: lift, $\beta[rad]$: bank angle,
$g[m/s^2]$: gravitational acceleration, C_L :lift coefficient,
C_D : drag coefficient, $q[Pa]$: dynamic pressure
$S_{ref}[m^2]$: reference area, $\mu[m^3/s^2]$: gravitational constant

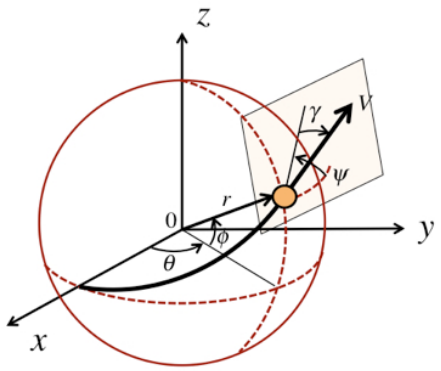

Fig. 3 The coordinates for the state equation

Initial ($t=t_0$) and terminal ($t=t_f$) condition are given as constraints as follows:

$$\begin{cases} C_0\left(\mathbf{x}(t_0),\mathbf{d}(t_0)\right)=\mathbf{0} \\ S_0\left(\mathbf{x}(t_0),\mathbf{d}(t_0)\right)<\mathbf{0} \end{cases} \tag{11}$$

$$\begin{cases} C_f\left(\mathbf{x}(t_f),\mathbf{d}(t_f)\right)=\mathbf{0} \\ S_f\left(\mathbf{x}(t_f),\mathbf{d}(t_f)\right)<\mathbf{0} \end{cases} \tag{12}$$

Equality and inequality constraints when flying in the atmosphere at an arbitrary time $t \in [t_0, t_f]$ are,

$$\begin{cases} C\left(\mathbf{x}(t),\mathbf{d}(t)\right)=\mathbf{0} \\ S\left(\mathbf{x}(t),\mathbf{d}(t)\right)<\mathbf{0} \end{cases} \tag{13}$$

Defining the variable vector and objective function vector as **X** and **J(X)**, respectively, optimization problem can be formulated as follows:

$$\text{Variables: } \mathbf{X}=\left[d_1(t),d_2(t),...,d_M(t)\right] \tag{14}$$

$$\text{Minimize: } \mathbf{J}(\mathbf{X})=\left[J_1(\mathbf{X}),J_2(\mathbf{X}),...,J_P(\mathbf{X})\right] \tag{15}$$

$$\text{Subject to: } \begin{cases} \mathbf{C}(\mathbf{X})=\begin{bmatrix} \dot{\mathbf{x}}(t)-f\left(\mathbf{x}(t),\mathbf{d}(t)\right) \\ C_0\left(\mathbf{x}(t_0),\mathbf{d}(t_0)\right) \\ C\left(\mathbf{x}(t),\mathbf{d}(t)\right) \\ C_f\left(\mathbf{x}(t_f),\mathbf{d}(t_f)\right) \end{bmatrix}=\mathbf{0} \\ \mathbf{S}(\mathbf{X})=\begin{bmatrix} S_0\left(\mathbf{x}(t_0),\mathbf{d}(t_0)\right) \\ S\left(\mathbf{x}(t),\mathbf{d}(t)\right) \\ S_f\left(\mathbf{x}(t_f),\mathbf{d}(t_f)\right) \end{bmatrix}<\mathbf{0} \end{cases} \tag{16}$$

Here, M and P are the number of design vectors and objective functions, respectively. The optimization problem for variable-geometry-aeroshell-aerocapture is to obtain the optimum time history of design vector **X** to minimize required objective function **J(X)** as well as satisfying the constraints **C(X)** and **S(X)**. This paper proposes the deformable aeroshell structure changed with dynamic pressure. The design variables of this system are only elasticity of aeroshell material and initial geometry of aeroshell, which is denoted by $\mathbf{d}(t_0)$. In other words, the aeroshell shape at arbitrary time depends on the initial shape $\mathbf{d}(t_0)$, elasticity of material, and dynamic pressure.

B. Variables

As a shape model for flexible aeroshell, axisymmetric thin flare-type aeroshell, which is composed of a conical membrane and an outer frame that supports aeroshell structure, is selected. It is assumed that outer frame can be inflated and deployed by injection of gas just like a "swimming tube", before entering the atmosphere. Design variable vector **d** is defined as the size in each part of this shape model. These are: 1) radius of flexible flare R_2, 2) angle of flexible flare θ_F, 3) radius of outer frame R_3, and 4) elasticity of material (Young's modulus) E_{mem}, as listed in Fig. 4. Here, radius of rigid nose R_1 is assumed to be 1.0 m. Boundaries of design variables are listed in (17) thorough (20).

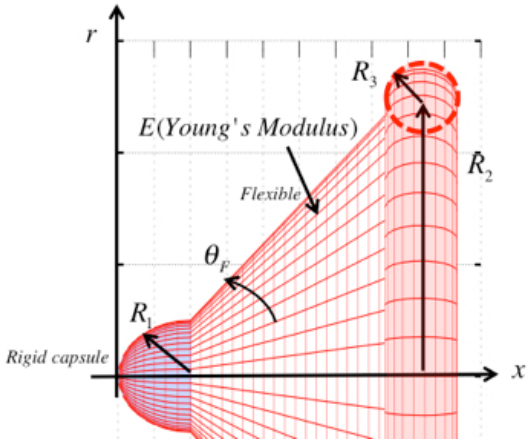

Fig. 4 Design variables

$$R_1 \le R_2[m] \le 12.0 \tag{17}$$

$$10.0 \le \theta_F[\text{deg}] \le 85.0 \tag{18}$$

$$0.1 \le R_3[m] \le 1.0 \tag{19}$$

$$1.0\times10^4 \le E_{mem}[Pa] \le 1.0\times10^9 \tag{20}$$

C. Objective Functions

In this paper, following objective functions are considered as expressed in (21) through (24). Firstly, objective function (21) aims to maximize the entry corridor width for the flexible, which is "deformation-use-type" vehicle. Here, $(\Delta\gamma)_{\text{deform}}$ is its entry corridor width. The important thing in this paper is comparing the corridor width of deformable type with "not-deformable type". With this in mind, secondary, objective functions (22) and (23) aim at maximizing the enlargement ratio of corridor against

not-deformed type. Here, $(\Delta\gamma)_{\text{not-deform1}}$ is the corridor in the case of always keeping the prior shape of deforming, without deforming throughout a flight. On the other hand, $(\Delta\gamma)_{\text{not-deform2}}$ is the corridor in the case of always keeping the posterior shape of deforming without deforming throughout a flight. In other words, these are the corridors in the case of flying with a constant aerodynamic coefficient as a rigid body. For example when a flexible vehicle changes its drag coefficient from 1.4 to 1.0 throughout the atmospheric flight, corridor $(\Delta\gamma)_{\text{not-deform1}}$ or $(\Delta\gamma)_{\text{not-deform2}}$ corresponds to the case of always keeping drag coefficient of 1.4 or 1.0, respectively. Thirdly, objective function (24) aims to minimize the maximum aerodynamic heating for deformation-use-vehicle. Here, surface temperature around rigid hemisphere part is evaluated assuming it as the same temperature at stagnation point. Heating rate at stagnation point is estimated by Tauber's relation [9], and surface temperature is assumed to become the radiation equilibrium temperature.

$$\max J_0(\mathbf{X}) = (\Delta\gamma)_{deform} \tag{21}$$

$$\max J_1(\mathbf{X}) = \frac{(\Delta\gamma)_{deform} - (\Delta\gamma)_{not-deform1}}{(\Delta\gamma)_{not-deform1}} \tag{22}$$

$$\max J_2(\mathbf{X}) = \frac{(\Delta\gamma)_{deform} - (\Delta\gamma)_{not-deform2}}{(\Delta\gamma)_{not-deform2}} \tag{23}$$

$$\min J_3(\mathbf{X}) = (T_{eq})_{\max} \tag{24}$$

D. Constraints

First one of constraints is expressed as inequality shown in (25). Inequality (25) explains that required mass which is sum of fuel, TPS, and structural mass, should not exceed the vehicle mass. *FUEL%*, *TPS%*, and *STRCT%* correspond to the fuel mass fraction, TPS mass fraction, and structural mass fraction, respectively. In order to insert the vehicle into target circular orbit shown in Fig.2, it is required to perform the maneuvering delta-V_1 and delta-V_2 burning at point 7 and point 8 by the orbital maneuvering engine (OME). Fuel mass fraction is evaluated by (26). The state of the art bi-propellant OME achieves an I_{sp} larger than 315 sec [1]. Practically, an OME, which realizes a much larger I_{sp}, may be able to be considered, but in this paper, I_{sp} of 315 sec is assumed as a conservative value. Required TPS mass per unit area on vehicle's nose, which is rigid hemisphere part, is evaluated using empirical relations shown in (27) and (28). It is known that the application limit of metal TPS is up to around 1500 K. Therefore, in this paper, it is assumed that ceramic tile is used when surface temperature is more than 1500 K, and on the other hand, metal TPS is used for less than 1500 K. Required structural mass is evaluated by the summation of membrane, outer inflatable frame, and gas, assuming that weight of membrane and outer inflatable frame per unit area are 0.1 kg/m^2 and 0.2 kg/m^2, respectively.

Second important constraint is structural strength of inflatable frame. According to a simple theoretical prediction, constraints on structural strength of inflatable frame can be expressed as (29) [10]. Symbols used in (29) are shown in Fig. 5. Equation (29) explains that if compressive force acting on the membrane surface due to the external force, that is denoted by $T_{out}\,sin\theta_{out}$, becomes more than the tensile force due to the inner pressure on the membrane of the inflatable frame, inflatable frame is locally collapsed, which is called as "local crippling". An example of local crippling collapsing mode is shown in Fig.6 [10]. Assuming that aeroshell is the ideal membrane without any initial imperfection and anisotropy, structural strength of inflatable torus agrees this simple theoretical equation.

$$S_1(X) = FUEL\% + TPS\% + STRCT\% - 1 < 0 \tag{25}$$

$$FUEL\% = 1 - \exp\left\{-(\Delta V_1 + \Delta V_2)/(gI_{sp})\right\} \tag{26}$$

$$ceramic\ tile\left[\frac{kg}{m^2}\right] = 0.0118 \times (T_{eq})_{\max} - 0.8833 \tag{27}$$

$$metal\ TPS\left[\frac{kg}{m^2}\right] = 0.01 \times (T_{eq})_{\max} \tag{28}$$

$$S_2(X) = T_{out}\sin\theta_{out} \cdot R_{out} - \pi r_{frame}^2 (P_{inner} - P_\infty) < 0 \tag{29}$$

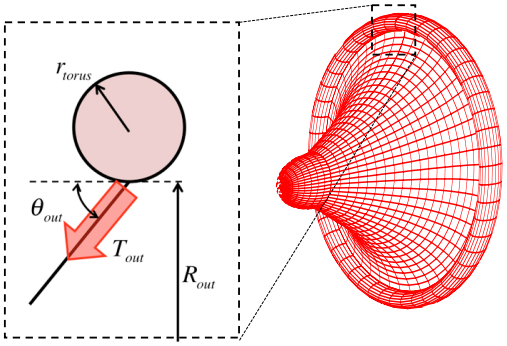

Fig. 5 Constraint on inflatable outer frame

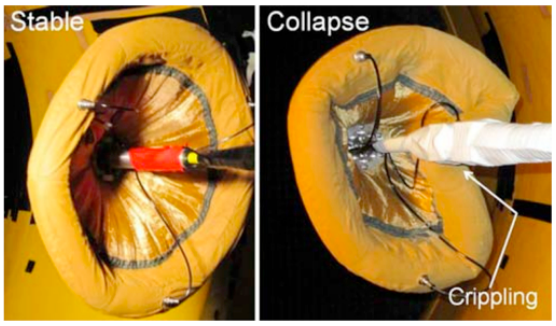

Fig. 6 Local Crippling collapse mode [10]

E. Aerodynamics and structural analysis model

The dynamics of flexible aeroshell and flow field are closely related with each other. The aerodynamic force deforms the shape of aeroshell, and deformation of aeroshell changes the flow field in turn. Here, as a fluid-structure interaction analysis model, a particle-based membrane model [11] is used. In this model, membrane is described

by a finite number of virtual particles as shown in Fig. 7. Deformation of aeroshell can be analyzed by solving the equation of motion for particles shown in (30). Here, forces acting on the particle located at position *(i,j)*, tensile force $(\mathbf{F}_T)_{i,j}$ aerodynamic force $(\mathbf{F}_A)_{i,j}$, and force caused by bending moment $(\mathbf{F}_B)_{i,j}$ are considered and c is damping coefficient of this system. Non-dimensionalization of (30) leads to (31). Here, ρ_∞, h_{mem}, and L_{ref} are the atmospheric density of uniform flow, thickness of flexible membrane, and reference length, respectively. It can be seen that the magnitude of deformation of membrane aeroshell is dominated by the non-dimensional parameter called C_{AE} as shown in (32). C_{AE} stands for the ratio of aerodynamic force to elastic force acting on membrane. In the optimization problem for flexible aeroshell, aerodynamic characteristics will be changed according to not only design variables **d**, but also aerodynamic-elasticity-coefficient C_{AE}.

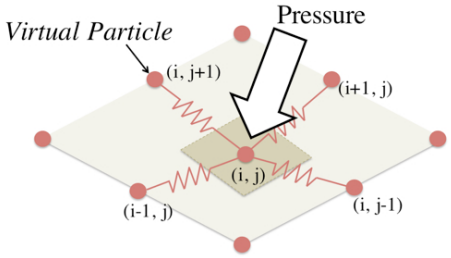

Fig. 7 Particle-based flexible membrane model

$$m_{i,j}\frac{d^2\mathbf{r}_{i,j}}{dt^2}+c\frac{d\mathbf{r}_{i,j}}{dt}=(\mathbf{F}_T)_{i,j}+(\mathbf{F}_A)_{i,j}+(\mathbf{F}_B)_{i,j} \quad (30)$$

$$\frac{d^2\hat{\mathbf{r}}_{i,j}}{d\hat{t}^2}+\hat{c}\frac{d\hat{\mathbf{r}}_{i,j}}{d\hat{t}}=\hat{C}\left\{(\hat{\mathbf{F}}_T)_{i,j}+\hat{C}_{AE}(\hat{\mathbf{F}}_A)_{i,j}+\frac{1}{12}\left(\frac{h_{mem}}{L_{ref}}\right)^2(\hat{\mathbf{F}}_B)_{i,j}\right\} \quad (31)$$

$$\hat{C}_{AE}\equiv\frac{1/2\rho_\infty V_\infty^2}{(h_{mem}/L_{ref})E_{mem}} \quad (32)$$

Considering the calculation cost of analyzing the aerodynamics, surface pressure on aeroshell is estimated by modified Newtonian theory [12]. Newtonian theory is appropriate for steady, continuum, inviscid flow, and its accuracy improves as Mach number of free stream M_∞ increases. As a conceptual design tool, it provides a reasonable approximation of the surface pressure distribution over hypersonic vehicle. Almost all flight conditions for aerocapture vehicle becomes hypersonic flow, thus its use is suitable here for estimating aeroshell aerodynamic characteristics. This theory models the flow as a stream of particles. Each particle impacts the surface and completely transfers its normal component of momentum to the surface. The particles in the free stream impact only on the frontal area of the body. They cannot curl around the body and also cannot impact on the back surface. Therefore, the pressure coefficient C_p is a function of the angle between the velocity vector and the unit vector normal to the panel of the body *ds* shown as (33). Here, $\mathbf{V}_\infty$ and $\mathbf{V}_{i,j}$ are, velocity vector of free stream, and velocity vector of particle located at position *(i,j)*, respectively. Strain occurred on membrane can be calculated by evaluating the distance of neighboring particles as shown in (34).

$$(C_p)_{i,j}=C_{p0}\left\{\frac{\mathbf{V}_\infty-\mathbf{V}_{i,j}}{|\mathbf{V}_\infty-\mathbf{V}_{i,j}|}\cdot\frac{d\mathbf{s}}{|d\mathbf{s}|}\right\} \quad (33)$$

$$(\varepsilon)_{i,j}=\frac{(\mathbf{l})_{i,j}-(\mathbf{l}_0)_{i,j}}{(\mathbf{l}_0)_{i,j}} \quad (34)$$

F. Optimization method

1. Multi-objective-Genetic-Algorithm

In order to evaluate the performance of flexible aeroshell aerocapture vehicle, it is important to consider its performance from various perspective of view because there are multiple items to be evaluated such as corridor enlargement ratio, fuel mass fraction (*FUEL%*), TPS mass fraction (*TPS%*), and structure mass fraction (*STRCT%*). These evaluation items should be treated simultaneously. Therefore, in this paper, multi-objective optimization is conducted by using Multi-Objective Genetic Algorithm [13]. Genetic algorithm (GA) is highly suitable to be used in multi-objective optimization because GA is multi-point search algorithm, and thus multiple Pareto optimal solutions can be captured in a single simulation run. On the other hand, conventional multi-objective optimization method, such as weighted linear combination method, requires tuning the weighting factors and multiple simulations. The Pareto optimal solutions are known as set of solutions which cannot but deteriorate at least one objective function value in order to improve a certain objective function value. In addition, GA does not require derivative or continuity of objective functions and constraints functions, therefore, it is expected to obtain the global solutions, and solutions are not sensitive to initial guess unlike derivative-dependent method. GA is imitating the evolution process of living things, and it consist of generating initial data set, evaluating the performance for each individual, selection, crossover, and mutation.

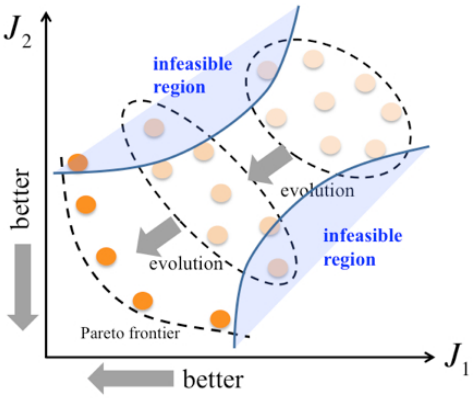

Fig. 8 Multi-Objective Genetic Algorithm

2. Response surface methodology

Aerodynamics and structural analysis for flexible aeroshell vehicle takes long time because behavior of deformation changes with respect to the changes in dynamic pressure, membrane materials, and design variables. It

means that aerodynamics and structure analysis should be executed for broad design variables' space and various C_{AE} values. That requires complicated and expensive analysis iteratively. Therefore, in this paper, aerodynamics and structural characteristics in the optimization process are evaluated by using the approximation model, which is called as response surface methodology [14]. Approximation model represents the relationship between design variables and response with simple equation. According to this methodology, relationship between sampled data set **X** and approximated response **f** can be expressed as shown in (35),

$$\mathbf{f}(\mathbf{X}) = \mathbf{g}(\mathbf{X}) + \varepsilon \tag{35}$$

where **f(X)** is the unknown (true) response of interest, **g(X)** is the approximated response, ε is random error assumed to be normally distributed with mean zero and variance σ^2. In this paper, Kriging interpolation model [15] is applied as a response surface model for following reasons: 1) assumption of order for interpolation curve is not necessary unlike spline or polynomial interpolation, 2) approximation error σ^2 of obtained response surface can be also estimated, and 3) Kriging technique is suitable for the case where there is no measurement error like the computer experiment, because it makes a surface that always passes through the sampled data point. Kriging methodology has originally developed in the field of geo-statistics to predict the spatial distribution of mineral resources. In recent years, it has been applied not only to the field of geology but also environmental science, aviation, material and so on [16]-[17].

The approximated drag coefficient by Kriging model for non-observed design variables $\mathbf{d}_0$ and C_{AE} of interest, which is denoted by $C'_D(\mathbf{d}_0, C_{AE})$ is assumed to be a weighted linear combination of the all the N obtained design variables vector, which is denoted by $C_D(\mathbf{d}_i, C_{AE})$, ($i$=1,2,…,$N$). In the GA process, N corresponds to the number of individuals.

$$C'_D(\mathbf{d}_0, C_{AE}) = \sum_{i=1}^{N} w_i C_D(\mathbf{d}_i, C_{AE}) \tag{36}$$

Here, w_i is weighting factor and the summation of w_i is required to be unity. The variance of estimation error σ^2 can be expressed by mean square error as shown in (37).

$$\sigma^2 = E\left[\left\{C'_D(\mathbf{d}_0, C_{AE}) - C^*_D(\mathbf{d}_0, C_{AE})\right\}^2\right] \tag{37}$$

$C^*_D(\mathbf{d}_0, C_{AE})$ is the true value at the point of non-observed design variables vector $\mathbf{d}_0$ and C_{AE} of interest, E[*] is the operator to calculate the mean value. Optimum w_i which minimizes the variance of estimation error σ^2, is determined by applying the Lagrangian multiplier method. This calculation results in the following system of linear equation,

$$\begin{bmatrix} \mathbf{G} & \mathbf{I} \\ \mathbf{I}^T & 0 \end{bmatrix} \begin{Bmatrix} \mathbf{w} \\ \lambda \end{Bmatrix} = \begin{Bmatrix} \mathbf{G}^* \\ 1 \end{Bmatrix} \tag{38}$$

where λ is the Lagrangian multiplier, **I** is the unit matrix, **G** corresponds to the variance-covariance-matrix composed of the all the N observed data, $\mathbf{G}^*$ corresponds to the variance matrix composed of the observed data and interested non-observed point $\mathbf{d}_0$. These are shown in (39) and (40).

$$\mathbf{G} = \begin{bmatrix} \mathrm{cov}(\mathbf{d}_1, \mathbf{d}_1) & \mathrm{cov}(\mathbf{d}_1, \mathbf{d}_2) & \cdots & \mathrm{cov}(\mathbf{d}_1, \mathbf{d}_N) \\ \mathrm{cov}(\mathbf{d}_2, \mathbf{d}_1) & \mathrm{cov}(\mathbf{d}_2, \mathbf{d}_2) & \cdots & \mathrm{cov}(\mathbf{d}_2, \mathbf{d}_N) \\ \vdots & \vdots & \ddots & \vdots \\ \mathrm{cov}(\mathbf{d}_N, \mathbf{d}_1) & \mathrm{cov}(\mathbf{d}_N, \mathbf{d}_2) & \cdots & \mathrm{cov}(\mathbf{d}_N, \mathbf{d}_N) \end{bmatrix} \tag{39}$$

$$\mathbf{G}^* = \begin{bmatrix} \mathrm{cov}(\mathbf{d}_1, \mathbf{d}_0) \\ \mathrm{cov}(\mathbf{d}_2, \mathbf{d}_0) \\ \vdots \\ \mathrm{cov}(\mathbf{d}_N, \mathbf{d}_0) \end{bmatrix} \tag{40}$$

In the Kriging model, covariance between two individuals $\mathbf{d}_i$ and $\mathbf{d}_j$, which is denoted by $\mathrm{cov}(\mathbf{d}_i, \mathbf{d}_j)$, is assumed that it depends only on the distance between them. Therefore, Kriging assumes that the closer the design variables are, the more positively correlated their responses are. The optimum weights for (36) can be obtained by solving above system of linear equation.

In this calculation, it is desired to arrange the sampled point to cover all the areas of solution space as much as possible. For this reason, as a space filling method, Latin Hypercube Sampling method [18] that is one of the design of experimental methodology is applied for generating initial design variables.

3. Calculation Process

Fig. 9 shows the calculation process. At first, initial design variables are generated using Latin Hypercube Sampling method. Secondarily, aerodynamics and structural analysis is executed using particle-based membrane model and Newtonian approximation for all sampled initial data set. In this phase, aerodynamic characteristics such as drag coefficient, strain and tensile force on membrane are obtained for following 8 cases of C_{AE}, these are 1.0×10^{-6}, 1.0×10^{-4}, 1.0×10^{-3}, 1.0×10^{-2}, 5.0×10^{-2}, 1.0×10^{-1}, 3.0×10^{-1}, and 5.0×10^{-1}. Thirdly, response surface against aerodynamic characteristics and structural strength are calculated by Kriging model using the aerodynamic calculation results of initial sample data set. Fourth, multi-objective optimization is executed. When executing trajectory analysis, aerodynamics of an evolved individual is approximated using obtained response surface. After the optimization, for the purpose of improving the accuracy of response surface, additional set of design variables are sampled and added to initial sample data set, and then response surface is calculated again. This process is repeated until solutions are converged or estimation error becomes allowable level.

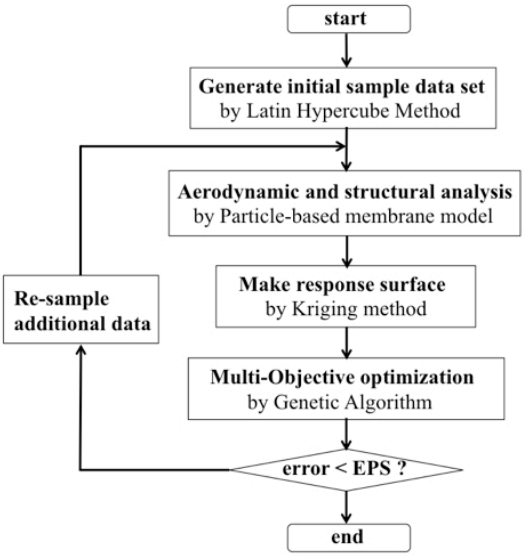

Fig. 9 Calculation process

III. Results

A. Discussion in objective functions space

Design optimization is conducted for 4 objective functions as previously given in (21) through (24), and 2 constraints (25) and (29). First of all, Fig.10 shows the generation history of distribution of individuals (solutions) projected in the objective functions J_0, J_1, and J_2. Distribution of individuals is progressing in the optimum direction of each objective functions as the GA generation is changed, thus the optimization calculation has been appropriately conducted and succeeded in investigating solutions. Fig.11 shows the comparison of corridor width between deformation-use type $(\Delta\gamma)_{def}$ and not-deformable-type-1 $(\Delta\gamma)_{not\text{-}deform1}$,which is in the case of always keeping the prior shape of deforming. Fig.12 shows the comparison of corridor width between deformation-use type $(\Delta\gamma)_{def}$ and not-deformable-type-2 $(\Delta\gamma)_{not\text{-}deform2}$,which is in the case of always keeping the posterior shape of deforming. For both cases, in the last generation, solutions are searched and converged in the domain which enables to achieve both maximization of corridor of deformation-use type (that is objective function J_0) and maximization of enlargement ratio of corridor (that is objective functions J_1 and J_2). As for the most superior solution, while $(\Delta\gamma)_{not\text{-}deform1}$ and $(\Delta\gamma)_{not\text{-}deform2}$ are 0.594 deg and 0.590 deg, and $(\Delta\gamma)_{def}$ is 0.656 deg, therefore the corridor can be enlarged up to 10.4 to 11.2%.

Fig.13 shows the relationship between corridor enlargement ratio, which is denoted by the objective function J_1, and maximum radiation equilibrium temperature at the stagnation point, which is denoted by the objective function J_3. As shown in Fig.13, maximization of J_1 and minimization of J_3 form the Pareto frontier. This is because in order to raise an enlargement ratio the vehicle tries to enter the atmosphere at a deeper entry angle and to fly through a lower altitude so that sufficient dynamic pressure to deform can be received. However, the slope of Pareto frontier is not so steep, that if the rise of about 80 K of aerodynamic heating is allowable, entry corridor can be enlarged by about 10%. In addition, maximum radiation equilibrium temperature for the solution J_1-optimum experiences about 970 K, which allows using reusable metal TPS. It is known that the application limit of using metal TPS is up to 1500 K. Therefore, the solution that utilizes its deformation is possible both to avoid aerodynamic heating and to get the robustness against error in entry angle.

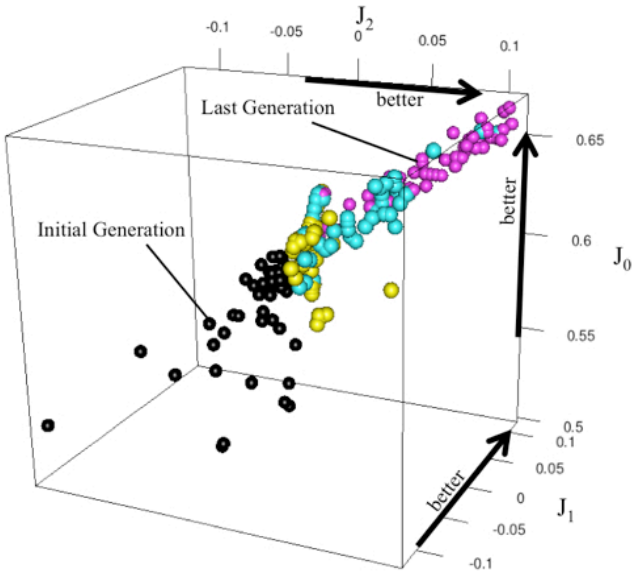

Fig. 10 History of distribution of solutions

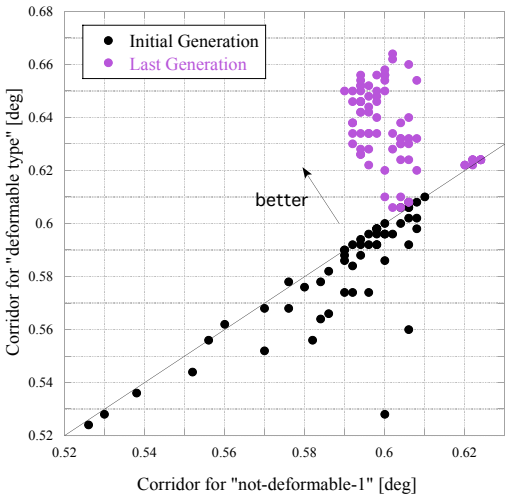

Fig. 11 Comparison of corridor between deformable type $(\Delta\gamma)_{def}$ and not deformable type 1 $(\Delta\gamma)_{not\text{-}deform1}$.

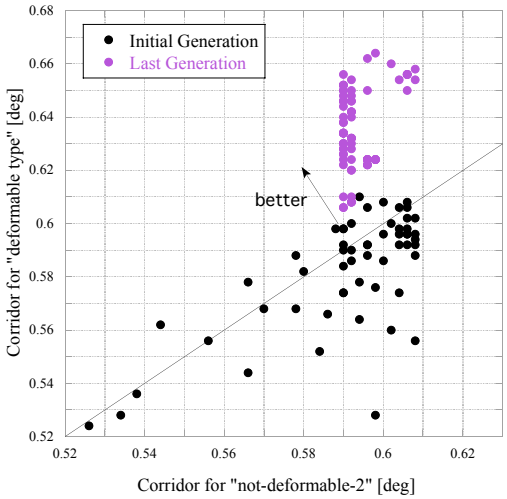

Fig. 12 Comparison of corridor between deformable type $(\Delta\gamma)_{def}$ and not deformable type 2 $(\Delta\gamma)_{not\text{-}deform\ 2}$

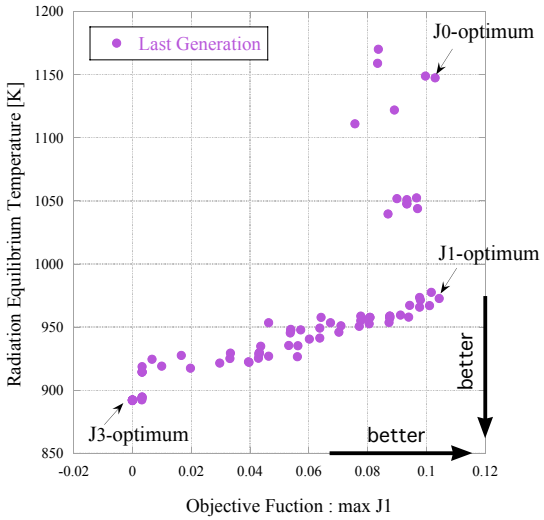

Fig. 13 Relationship between objective function J_1 and J_3

B. Discussion in design variables space

Fig.14 shows the relationship among angle of flexible flare θ_F and objective functions J_1 and J_3 obtained at the last generation of optimization. The solutions that aim to minimize objective function J_3 converge at the upper boundary of θ_F defined as 85 deg. This is reasonable because as θ_F increases drag coefficient is also increased. On the other hand, the solutions that aim to maximize objective function J_1 are distributed around 60 to 70 deg. These solutions change its drag coefficient from 1.6 to 1.1. This result shows that optimum initial drag coefficient for maximization of enlargement ratio is 1.6.

Fig.15 shows the relationship among elasticity of membrane called Young's modulus E_{mem} and objective functions J_1 and J_3 obtained at the last generation of optimization. The solutions that aim to minimize objective function J_3 converge at the upper boundary of E_{mem} defined as 1.0×10^9 Pa. The solutions of J_3-optimum tend to keep drag coefficient as high as possible to decelerate at higher altitude, therefore the infinitely high elasticity was chosen to prevent from deforming and decreasing drag coefficient. On the other hand, the solutions that aim to maximize objective function J_1 tend to be distributed around the order of 10^6 Pa. Too low elasticity provides too early deformation, on the other hand, too high elasticity does not allow deformation. The optimum combination of design variables was chosen as the one that gives the optimum time history of change in aerodynamic coefficient which can provides the effect of deformation maximally during flight.

Fig.16 shows the relationship between elasticity E_{mem} and maximum radiation equilibrium temperature for following 3 parts of vehicle: on the membrane, outer frame, and stagnation point (this is objective function J_3) obtained at the last generation of optimization. Here, it is assumed that the influx of heat rate per unit area to membrane and outer frame are, 60% and 40% of that at stagnation point. In addition, as for membrane, heat can be radiated from both sides, and its emissivity is assumed to be 0.9. With regard to outer frame, because temperature of the fluid inside the inflatable frame is unknown, supposing the worst case, it is assumed that heat can be radiated only from one side. Fig.16 shows that deformable vehicle requires the membrane of which elasticity is order of 10^6 Pa and upper temperature limit is around 700 K.

With regard to the deformation-use-type solutions (J_1 and J_2-optimum) and the temperature-minimizing solutions (J_3-optimum), the aerodynamic characteristics and maximum strain occurred in membrane and aeroshell shape, extracted as typical solutions, are shown in Fig.17 and Fig.18 (a)(b). In Fig.19, shape deformation and change in distribution of pressure coefficient along with increase of dynamic pressure for deformation-use-type solutions (J_1 and J_2-optimum) is shown. As shown in Fig.17 and Fig.19, drag coefficient for J_1 and J_2-optimum can be decreased from 1.61 to 1.15 by trailing the aeroshell and lowering surface pressure, being adapted for the rise of dynamic pressure. Drag coefficient is rapidly changed when C_{AE} becomes 1.0×10^{-2} or more. The case of J_3-optimum also decreases drag coefficient from 1.8 to 1.3, but Young's-modulus of J_3-optimum is chosen as large enough value, J_3 optimum does not deform and thus it is able to keep drag coefficient of 1.8 throughout the atmospheric flight. Maximum strain, which occurs at the root of membrane, is also changed, from 0% to 200%.

As an example of trajectory, the time history of altitude for J_1 and J_2-optimum solution is shown in Fig.20. In Fig.20, the trajectory of not-deformable-type-1, which does not deform at all and keeps the prior shape, is also shown. Although entry angles for both cases are -6.9 deg, not-deformable-type-1 resulted in failure, but deformable-type (J_1 and J_2-optimum) succeeded in completing aerocapture, owing to its deformation effect. This effect can be seen in Fig.21, which is time history of drag force, and Fig.22, which shows drag force against C_{AE} that vehicle experiences throughout atmospheric flight. As vehicle lowers altitude, dynamic pressure thus C_{AE} becomes large and it deforms its shape so that drag coefficient is decreased. Resultant drag force is reduced and it prevents the vehicle from too much deceleration. In this flight, C_{AE} reaches up to 0.3, therefore maximum strain becomes 120%.

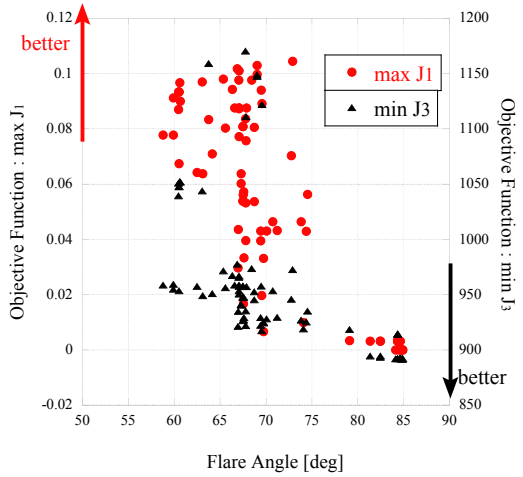

Fig. 14 Relationship among θ_F and objective functions J_1 and J_3

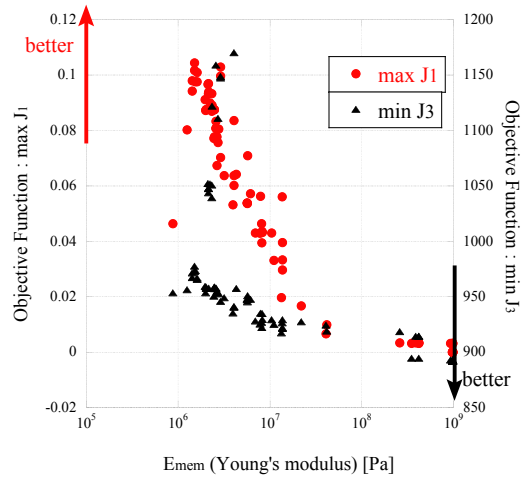

Fig. 15 Relationship among E_{mem} and objective functions J_1 and J_3

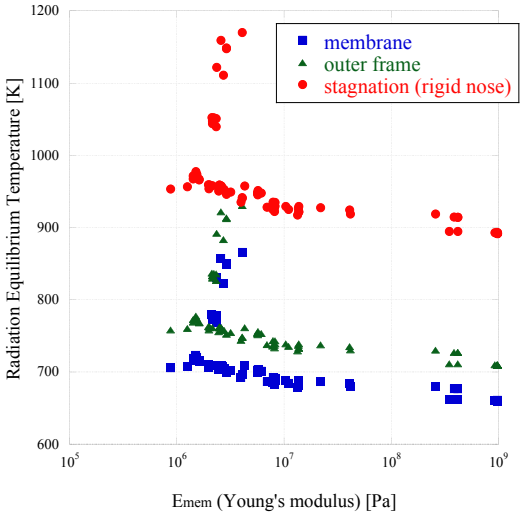

Fig. 16 Relationship among E_{mem} and radiation equilibrium temperature for 3 parts of vehicle

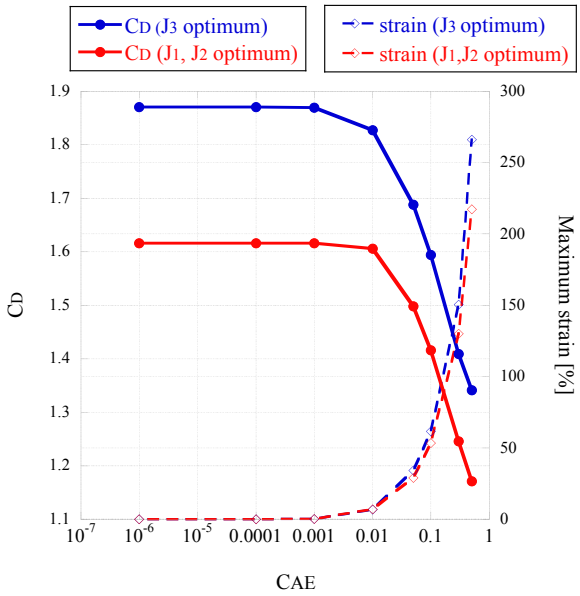

Fig. 17 Aerodynamic coefficient and maximum strain occurred in membrane for J_1 and J_2-optimum and J_3-optimum

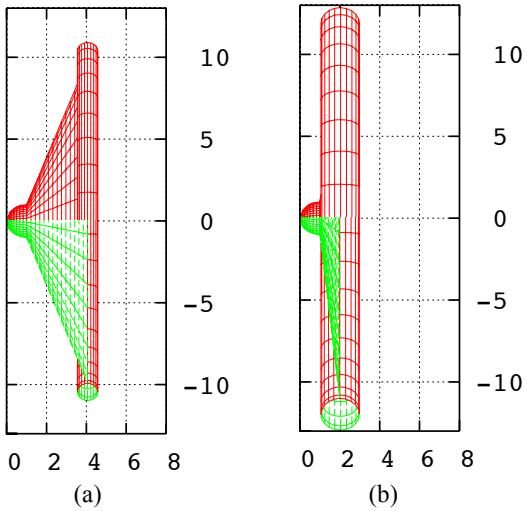

Fig. 18 Aeroshell shape
(a) J_1 and J_2-optimum (b) J_3-optimum (unit:[m])

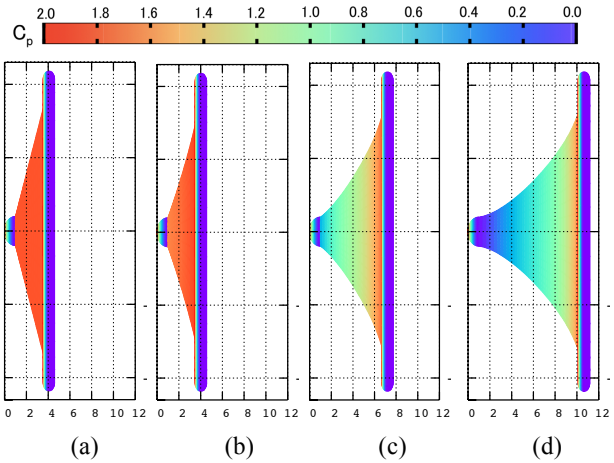

Fig. 19 Shape deformation and distribution of pressure coefficient for J_1 and J_2-optimum (a) C_{AE}=1.0×10^{-6}, (b) C_{AE} =1.0×10^{-3}, (c) C_{AE} =1.0×10^{-1}, (d) C_{AE} =3.0×10^{-1}

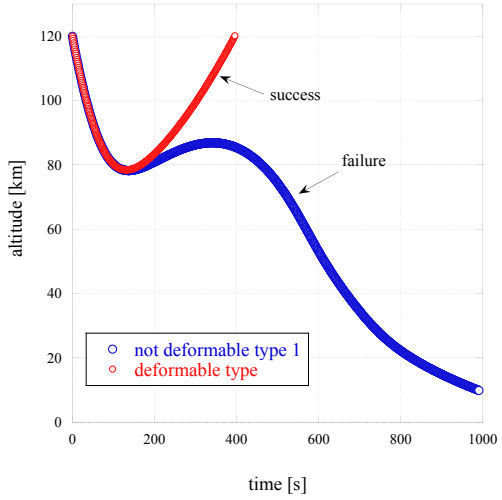

Fig. 20 Time history of altitude for deformable-type and not-deformable-type-1 (J_1 and J_2-optimum)

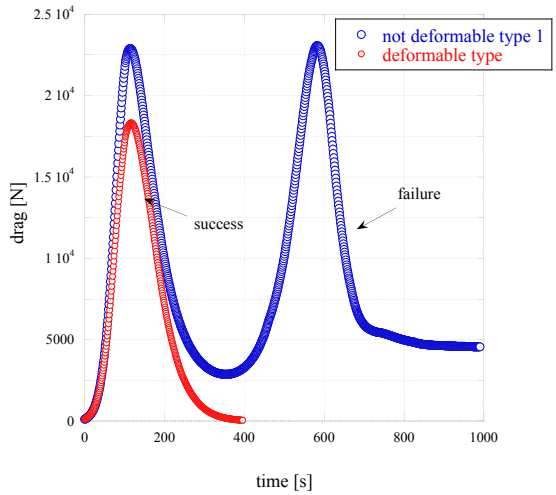

Fig. 21 Time history of drag force for deformable-type and not-deformable-type-1 (J_1 and J_2-optimum)

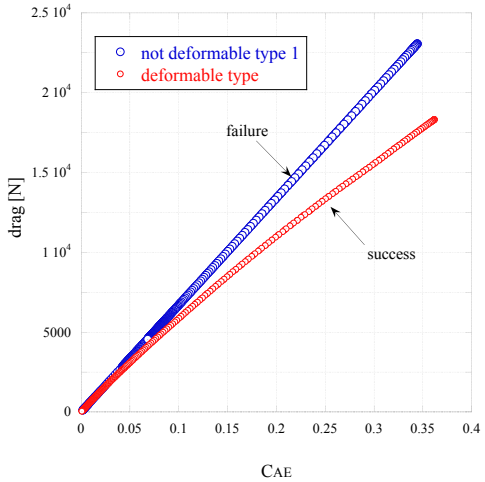

Fig. 22 Drag force against C_{AE} for deformable-type and not-deformable-type-1 (J_1 and J_2-optimum)

IV. Conclusion

In this paper, the design concept of aerocapture with aerodynamic-environment-adaptive variable geometry flexible aeroshell, deploys the flexible membrane as its aeroshell, is proposed in order to solve problems obstructing realization of aerocapture technique. This becomes a complicated design problem because multi-disciplinary domains such as aerodynamics, structure, and trajectory are related with each other closely, thus deriving the design guidelines is an important requirement. Multi-objective optimization study is conducted to understand solution space and to search solutions avoiding aerodynamic heating and having robustness against error in entry angle. Optimization problem using particle based membrane model, genetic algorithm and response surface methodology is formulated considering for following objective functions: maximization of entry corridor, maximization of corridor enlargement ratio, and minimization of maximum equilibrium temperature at stagnation point. As a result, the solutions that achieve both avoiding aerodynamic heating and having robustness for entry angle are obtained. Corridor can be enlarged about 10 to 11% at maximum, as a result of shape deformation. Maximization of corridor enlargement ratio and minimization of maximum radiation equilibrium temperature becomes trade-off relationship, but Pareto frontier is not so steep, that with rise of 80 K of aerodynamic heating is allowable, entry corridor can be enlarged by about 10%. Deformation-use-type solutions change its drag coefficient from 1.6 to 1.1, along with the change in C_{AE} up to around 0.3. Resultant drag force is reduced by deformation, thus over deceleration can be avoided. In addition, while elasticity of order of 10^6 Pa was chosen as optimum for them, temperature-minimizing solutions tend to choose infinitely large elasticity to prevent from decreasing drag coefficient. Moreover, deformation-use-type solutions requires the membrane of which upper temperature limit is more than 700 K, and upper strain limit is more than 120 %.

Acknowledgment

This work is supported by Grant-in-Aid for JSPS Fellows of Japan Society for the Promotion of Sciences, Grant Number 11J03277.

References

[1] T. Matsuo, K. Morishima, R. Inoue, and Y. Nonaka, “Development of 500N Ceramic Thruster for a Venus Explorer ‘Planet-C’ ”, *Mitsubishi Heavy Industry Technical Review*, vol.45, pp.46-49, 2008

[2] Gerald, D. Walberg. “A Survey of Aeroassisted Orbit Transfer”, *J. Spacecraft and Rockets*, vol.22, pp.3-18, 1985

[3] Zumwalt, C. H., Sostaric, R. R., and Westhelle, C. H., “Aerocapture Guidance and Performance at Mars for High-Mass Systems”, AIAA paper 2010-7971, AIAA/AAS Astrodynamics Specialist Conference, Toronto, Canada. 2010.

[4] K. Yamada, T. Abe, K. Suzuki, O. Imamura, D. Akita, and MAAC R&D Group, “Reentry Demonstration Plan of Flare-type Membrane Aeroshell for Atmospheric Entry Vehicle using a Sounding Rocket”, AIAA paper, 2011-2521.

[5] K. L. Daniel, et al, “Inflatable Re-entry Vehicle Experiment (IRVE)-4 Overview”, AIAA paper, 2011-2580.

[6] R. Philippe, E. David, ”Postflight Analysis of Inflatable Reentry and Descent Technology Blackout During Earth Reentry”, *J. Spacecraft and Rockets*, vol.46, pp.800-809, 2009

[7] M. Shibahara, T. Kida, "*Introduction to the Space Engineering (in Japanese)*", Tokyo: Baifukan, 1998, pp. 117-128
[8] M. M. Michelle, "Overview of the NASA Entry, Descent, and Landing System Analysis (EDL-SA)", 7th international Planetary Probe Workshop, 2010.
[9] Tauber, M. E., Bowles, J. V. and Yang, L., "Use of Atmospheric Braking during Mars Mission", *J. Spacecraft and Rockets*, vol.27, pp.514-521, 1990.
[10] K. Yamada, T. Sonoda, K. Nakashino, and T. Abe, "Structural Strength of Flare-type Membrane Aeroshell Supported by Inflatable Torus against Aerodynamic Force", the 28th International Symposium on Space Technology and Science, 2011-c-34, 2011.
[11] Yamada, K., and Suzuki, K., "A Particle-Based Model and Its Validation for Deformation Analysis of Membrane Aeroshell *(in Japanese)"*, *JSASS*, vol.53, pp.51-60, 2005.
[12] Anderson, J. D. Jr., "Hypersonic and High Temperature Gas Dynamics", New York: McGraw-Hill, 1989, pp.45-56.
[13] Deb. K., Agarwal. S., Pratap. A, and Meyarivan. T., "A Fast and Elitist Multiobjective Genetic Algorithm: NSGA-2", *IEEE Transactions on Evolutionary Computation,* vol.6, pp.182-197, 2002
[14] Box, G. E. P., Wilson, K. B., "On the experimental attainment of optimal conditions", *J. Royal Statistical Society*, vol.13, pp.1-45, 1951.
[15] Timothy,W.S., et al., "Kriging Models for Global Approximation in Simulation-Based Multidisciplinary Design Optimization", *AIAA Journal*, vol.39, pp.2233-2241, 2001.
[16] M.Kanazaki, S.Jeong, and K.Yamamoto, "High-Lift System Optimization Based on Kriging Model Using High Fidelty Flow Solver", Transactions of The Japan Society for Aeronautical and Space Sciences, vol.49, pp.169-174, 2006.
[17] M.Sekishiro, A.Todoroki, "Dimension and Stacking Sequence Optimization of Large Composite Structures Using Kriging and MOGA Method", Journal of the Society of Materials Sciences Japan, Vol.56, No.5, pp.432-437, 2007.
[18] M. D. Mckay, W. J. Conover., "A Comparison of Three Methods for Selecting Values of input Variables in the Analysis of Output from a Computer Code", *Technometrics*, vol.21, pp.239-245, 1979.